CIWEM Chartered Institution of Water and Environmental Management · Journal of **Flood Risk Management** **WILEY**

ORIGINAL ARTICLE

Two-dimensional hydrodynamic modelling for urban flood risk assessment using unmanned aerial vehicle imagery: A case study of Kirsehir, Turkey

Emrah Yalcin 🔟

Department of Civil Engineering, Kirsehir Ahi Evran University, Kirsehir, Turkey

Correspondence
Asst. Prof. Dr Emrah Yalcin, Department of Civil Engineering, Kirsehir Ahi Evran University, 40100 Kirsehir, Turkey.
Email: emrah.yalcin@ahievran.edu.tr

This study is an assessment of flash flood risk in the downstream part of an intermittent stream which lost its natural bed due to intense human interventions, with the example of Hastane Brook in the province of Kirsehir (Turkey). The effects of flooding events with high, medium, and low probability of occurrence are investigated on a street-by-street basis with a two-dimensional (2D) hydrodynamic model constructed in HEC-RAS 5.0 software. Due to the lack of records of past flood events required for model calibration, it is aimed to utilise high-quality data as much as possible in model development. Therefore, to more accurately simulate the movement of water and thereby to advise adequate measures for reducing the most likely flood effects, the required high-resolution terrain and land use data are produced by processing the aerial images acquired by the unmanned aerial vehicle (UAV) flights over the flood risk zone. The estimation of flood hydrographs is only based on the synthetic unit hydrograph methods due to the absence of representative stream gauging stations inside or near the region. The resultant flood hazard maps are cautionary in terms of demonstrating the effects of possible floods that are unexpected to come from such an intermittent stream basin.

KEYWORDS
2D hydrodynamic modelling, flash flood, HEC-RAS 5.0, Kirsehir, synthetic unit hydrograph, Turkey, UAV imagery, urban flooding

1 | INTRODUCTION

Floods are arguably the most devastating, widespread, and frequent natural disasters responsible for significant loss of lives and property throughout the world. Although floods themselves are natural phenomena that always have occurred and will always continue to occur in the future, it is urbanisation and settlement in flood prone areas that transfers them into disaster. In recent years, disastrous floods have become more frequent and intense, and this tendency is likely to be amplified in the future due to climate warming and ever-increasing human activities on natural floodplains (Dankers & Feyen, 2009). Therefore, while these events themselves cannot be prevented, their disastrous consequences can be minimised by taking appropriate flood risk mitigation measures.

For assessing flood management strategies, it is important to analyse historical floods based on in-situ observations. However, such records are not always available, especially for flash flood events. This type of flooding is triggered by local intense rainstorm events and leads to short-term inundations (less than 24 hr) of small urbanised areas at the downstream of tributary catchments such as low-lying parts of a city surrounded by rugged hills and mountainous (Sen, 2018). Rapid inundation process and cloudy skies during this period limit the use of remote sensing data

to obtain observation-based flood extent delineation. Besides, the increasing proportion of impervious urban lands to pervious agricultural areas and open spaces in growing cities limits the use of existing historical data that are valid only for the topographic conditions at the time of the event. Therefore, flash flood occurrences are highly problematic to propose flood management measures due to the limited information on them and faster reactions of their watercourses to precipitation events.

Flash floods are more common in arid and semiarid regions with steep topography and weak vegetation (Sen, 2018). Occasional very intense and often short-duration precipitations over these arid areas rapidly produce large volumes of flood water moving at speeds more than 1.5 m/s, faster than a person can escape, along mostly dry watercourses draining mountains (Dein, 1985). Flash floods are highly risky occurrences that are difficult to predict and occur suddenly without any warning signs (Zevenbergen et al., 2010). However, due to long intervals between flooding events, the lack of historical flood disaster records and growing need for new settlement areas due to urban expansion, land developers, and local population has paid relatively little attention to these natural processes ignoring sudden potential hazard risks to human life and property (Ghoneim & Foody, 2013). Hence, continuing urban development in such flood prone areas makes it necessary to prepare flood hazard maps indicating safe and unsafe regions under potential flash flood scenarios.

With the advancement of computational technology, many one-dimensional (1D), two-dimensional (2D), 1D/2D coupled, and three-dimensional (3D) numerical models with different capabilities have been developed to simulate the flow dynamics and extent of possible flooding events. Although 1D hydrodynamic models could be useful to simulate flooding in channels and open surface floodplain areas, they present several limitations for inundation analyses in topographies with complex geometries. Besides, complex 3D representation of flow dynamics is not viable at large scales, being time consuming with relatively low efficiency. Hence, the use of 2D hydrodynamic models would be adequate to resolve complex inundation processes on urban topographies under 2D shallow water approximation (Liu, Qin, Zhang, & Li, 2015; Quiroga, Kure, Udo, & Mano, 2016; Teng et al., 2017).

Flood modelling process and mapping results are influenced by several sources of uncertainty such as inputted data, model structure, and model parameters (Papaioannou, Loukas, Vasiliades, & Aronica, 2016). Generally, 2D models simulate the distribution of velocity and water depth over the extent of flooded area across a grid or mesh structure that defines topographic information according to flood hydrographs inputted as upstream boundary condition (Anees et al., 2016; Quiroga et al., 2016). An important source of uncertainty affecting the resulting distribution of velocity and water depth especially over the extent of

complex floodplains built by these simulation models is the quality of inputted digital surface model (DSM). Several studies have demonstrated that a high-resolution DSM with sufficient vertical accuracy is a prerequisite to more accurately resolve the detailed and complex flow structure of a possible flood event on an urban topography (Casas, Benito, Thorndycraft, & Rico, 2006; Cook & Merwade, 2009; Sanders, 2007; Schumann et al., 2008; Smith, Edwards, Priestnall, & Bates, 2006; Tsubaki & Fujita, 2010).

In recent years, the advances in remote sensing technology lead to generate high-resolution DSMs that will significantly improve the accuracy of hydraulic models. It is possible to produce high-quality DSMs with vertical accuracies of 10 cm using 0.5 m resolution satellite imageries (e.g., WorldView-2 and GeoEye). Besides, the airborne light detection and ranging (LiDAR) technology could provide 0.1 m resolution DSMs with vertical accuracies of 25 cm, depending on terrain features, flight parameters, and environmental conditions (Els & Van Niekerk, 2013). However, these technologies are quite expensive for mapping relatively small areas, and the needed imagery cannot be provided immediately due to their dependence on cloud conditions. The unmanned aerial vehicle (UAV) photogrammetry is a valuable solution in production of high-quality topographic data with centimetre-scale accuracies due to its advantages on rapid acquisition of high-spatial-resolution images, cost-effectiveness, and high temporal resolution (Colomina & Molina, 2014). UAV-based aerial photography has widely utilised in several hydrological studies on topographic measurements and monitoring of natural hazards (Feng, Liu, & Gong, 2015; Langhammer, Bernsteinova, & Mirijovsky, 2017; Serban et al., 2016).

The objective of this study is to analyse flash flood risk of the Kirsehir city center from an intermittent stream in the semi-arid mountainous region surrounding the northern part of the city. Topographic data required in representing flow structure on a street-by-street basis is produced by processing the aerial images acquired by UAV flights over the flood risk zone. Flood scenarios with high, medium, and low probability of occurrence are generated by estimating flood hydrographs with synthetic unit hydrograph methods using the observed annual maximum 24-hr precipitation values. For these scenarios, inundation processes in the city center are simulated with a 2D hydrodynamic model constructed in HEC-RAS 5.0 software (US Army Corps of Engineers Institute for Water Resources Hydraulic Engineering Center, Davis, California) using a combination of UAV and terrestrial surveys to characterise floodplain resistance. Flood hazard maps are prepared with the characteristics of flood extents, water depths, flow velocities, and arrival times obtained in the unsteady flow simulations for recurrence flood hydrographs. These maps form the basis for the adoption of structural and non-structural measures to be implemented for the minimization of the damage potential for this flood-prone area.

2 | STUDY AREA

Kirsehir province is in the Central Anatolia Region of Turkey. The northeastern part of the Kirsehir city center, between the latitudes 39°09′50″ and 39°08′10″N, and the longitudes 34°09′10″ and 34°10′20″E, faces flood risk from Hastane Brook coming from the mountainous region in the north of the city. Hastane Brook is an intermittent stream that flows only several days each year. It drains an area of about 11 km² from its source to the region where buildings are located, as demonstrated in Figure 1. In the past years, its flow route to Kilicozu Creek was blocked by the construction of the Ankara-Kayseri road (D260), and after this point, the streambed was completely disappeared because of the intensive construction of buildings and roads in this flood risk zone. Hence, in a possible flooding, runoff coming from this semi-arid mountainous watershed will pass the intercity road and head directly towards the city center.

The last major flood event from this mountainous region occurred in 1989, resulting in the inundation of 20 buildings according to the preliminary investigation report on the flood protection strategy of the Kirsehir city center. In this report, it is advised that the stream should be directed into a concrete channel extending up to Kilicozu Creek (DSI, 1989). However, to date, no structural and non-structural measures have been taken to reduce inevitable flood impacts, and the number of buildings in this region has further increased. Besides, there is not a sufficient rainwater drainage system in this floodplain area, like the other parts of the city center.

Other than this report, there is no flood data including observed water levels and extents of past flood events. Even if there were such records, it would not be correct to use them in a flood risk assessment for the present situation due to the major changes in the topography of the flood risk zone, such as the Hastane overpass on the D260 road build in 2015. This structure is located on the flow route of the stream affecting the movement of water to the city center. Therefore, the risky area that could be exposed to a possible flood event from Hastane Brook is roughly determined as 3.24 km², which is about 60% of the city center. In this complex urbanised area, there are many critical structures such as hospitals, schools, playgrounds, public institutions, and mosques together with heavy vehicle and pedestrian traffic.

3 | METHODOLOGY

The framework for the preparation of flood hazard maps to demonstrate the severity of damage that may occur with possible potential flood events from Hastane Brook in the city center of Kirsehir consists of three main stages: (a) estimations of flood hydrographs, (b) generation of a
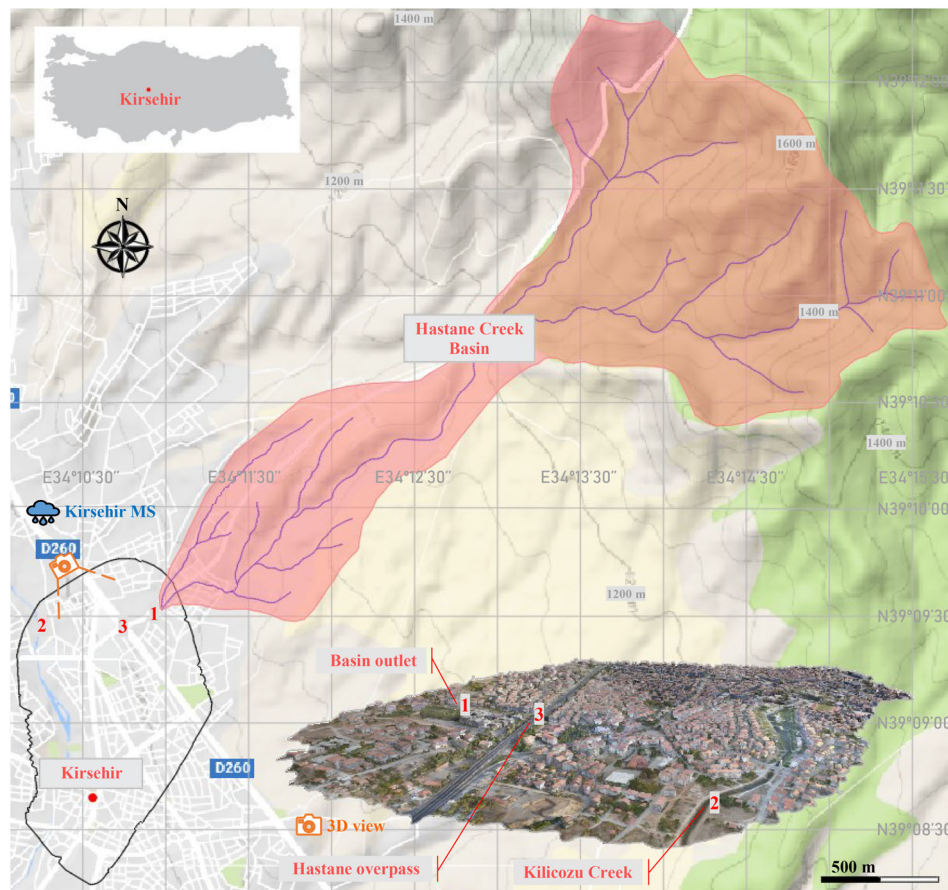

FIGURE 1 Description of the study area

high-resolution DSM, a georeferenced orthophoto and a land cover map of the flood risk zone, and (c) examination of possible flood hazards with 2D hydrodynamic model analyses.

3.1 | Determination of recurrence flood hydrographs using synthetic unit hydrograph methods

The 50-, 100- and 500-year flood hydrographs are estimated using the superposed Mockus and DSI synthetic unit hydrograph methods. These methods differ generally from each other in terms of the equations used in calculating peak discharge, time to peak discharge, and base time values of unit hydrographs to be generated. The Snyder's method is not performed because the subject catchment is smaller than 1,000 km^2 (Ozdemir, 1978; Usul, 2009). Moreover, recurrence flood peaks cannot be calculated statistically using point and regional flood frequency analyses due to the absence of representative stream gauging stations inside or near this region. Hence, the results of the synthetic method providing higher flood discharges is utilised in the modelling part of the study.

3.1.1 | Precipitation analysis

Flood analysis is based on the 74 year-precipitation records from 1942 to 2015 of the Kırsehir meteorological station operated by the Turkish State Meteorological Service (MGM), shown in Figure 1 (MGM, 2017a). To calculate 24-hr precipitation for different return periods, the log-Pearson type 3 distribution is selected as the best fitting frequency distribution to the annual maximum 24-hr precipitation rates of this station according to the Kolmogorov–Smirnov test. There is no other representative meteorological station inside or near the Hastane Brook basin to be used in obtaining mean areal precipitation through Thiessen polygons. Therefore, the corrected and maximised rainfall magnitudes of the subject basin for different return periods are determined directly by multiplying the calculated daily precipitations of the Kirsehir station by the pluviograph coefficients of the station, the areal distribution coefficients of rainfall of the basin, and the maximisation factor, 1.13, as advised by the General Directorate of State Hydraulic Works (DSI) (Eren, 2011; Ozdemir, 1978).

3.1.2 | Unit hydrograph analysis

The key parameters in the derivation of synthetic unit hydrographs as drainage area, hydraulic length of the watershed, distance from the basin outlet to a point on the main stream nearest to the centroid of the drainage area, and harmonic slope of the main stream are measured on the 1:25,000 scale digitised topographic maps of the region. Substitution of these parameters into the Mockus synthetic unit hydrograph method gives a 0.5-hr triangular hydrograph with a peak discharge of 2.54 m^3/s, a time to peak discharge of 0.81 hr and a base time of 2.43 hr. In the DSI synthetic unit hydrograph method, peak discharge, time to peak discharge, and base time values are determined as 1.20 m^3/s, 1.88 and 9.39 hr, respectively, and a 2-hr hydrograph is drawn for this watershed using the dimensionless unit hydrograph coordinates of the DSI method (Ozdemir, 1978). The details of these computations are summarised in Table 1.

3.1.3 | Flood hydrographs

The critical precipitation duration for this basin is determined to be 4 hr from the map showing regional critical precipitation durations for the whole country (Ozdemir, 1978). The precipitation amounts falling during this critical precipitation duration are subdivided into unit hydrograph blocks using the precipitation distribution curve of type A for the Mockus method. In the flood hydrograph computations based on the derived DSI synthetic unit hydrograph, a special precipitation distribution curve that is valid for the whole country is utilised as advised by Ozdemir (1978). To estimate excess rainfall that is the portion of the measured rain generating runoff, the SCS method is applied. The SCS curve number is evaluated as 82 according to the topography, plant cover, land use, soil type, and slope of the watershed (DSI, 1989). Then, hydrographs for different return periods are determined using the unit hydrograph method.

According to the records of the Kirsehir station for the period 1960–2016, the mean annual number of days with snow cover is about 25, and the monthly mean snow depth in winter from December to March is only about 5 cm (MGM, 2017b). Hence, a notable snowmelt contribution to runoff cannot be mentioned in the watershed. Besides, as a result of the periodic site investigations for about 2 years, it is observed that there is not continuous water flow in Hastane Brook throughout the year. The knowledge derived from the conducted interviews with locals also confirms this state. Therefore, any baseflow and snowmelt runoff are not added to the resultant flood hydrographs to be used in the 2D hydrodynamic flood analyses. The 50-, 100-, and 500-year flood hydrographs obtained with synthetic unit hydrograph methods are presented in Figure 2. Although both methods lead to reasonable results, the flood discharges of the Mockus method are higher than the ones of the DSI method. Hence, the results of the Mockus method are utilised in the modelling part of the study to be on the safe side in determining flood risk zones of the city center.

3.2 | Generation of high-resolution DSM and land cover map using UAV-based aerial photography

The use of UAV technology for producing high-quality topographic data is an appropriate solution for this assessment since LiDAR or satellite-based remote sensing techniques cannot be implemented due to cost issue. The UAV-based framework for generating the required DSM of this flood risk zone consists of three steps: establishment of

TABLE 1 Basin characteristics and derivation of synthetic unit hydrographs

Item	Unit	Definition	Formula	Explanations	Value
Basin characteristics					
A	km^2	Drainage area	–	–	11.08
L	km	Hydraulic length of the watershed	–	–	7.43
L_c	km	Distance from the basin outlet to a point on the main stream nearest to the centroid of the drainage area	–	–	4.74
S_h	–	Harmonic slope of the main stream	$S_h = \left(p/\sum_{i=1}^{p} \sqrt{\frac{1}{\sqrt{S_i}}} \right)^2$	Where p is the total number of divided segments and S_i is the slope of the divided segment.	0.054
ΔH	m	Elevation difference between the upstream and downstream ends of the watershed	–	–	515
CN	–	Curve number	–	–	82
S	mm	Potential maximum retention after runoff begins	$S = (1000/CN - 10) * 25.4$	–	55.76
Mockus synthetic unit hydrograph					
T_c	hr	Time of concentration	$T_c = 0.00032 * (L * 1000)^{0.77}/S_h^{0.385}$	–	0.94
ΔD	hr	Unit rainfall duration	$\Delta D \leq T_c/5$	For $T_c < 3$, ΔD should be taken as 0.50.	0.50
T_p	hr	Time to peak discharge	$T_P = 0.5 * \Delta D + 0.6 * T_c$	–	0.81
K	–	Basin parameter #1	$K = 0.201 + 0.01183*L/\sqrt{A} - 0.2646*\Delta H/(1000*\sqrt{A})$	–	0.186
H	–	Basin parameter #2	$H = (2 * 0.278 - K)/K$	–	1.982
T_r	hr	Time of recession	$T_r = H * T_p$	–	1.61
T_b	hr	Base time	$T_b = T_p + T_r$	–	2.43
Q_p	$m^3 s^{-1} mm^{-1}$	Peak discharge	$Q_p = K * A * h_a/T_p$	h_a is the unit rainfall depth which is 1 mm.	2.54
DSI synthetic unit hydrograph					
q_p	$1 s^{-1} km^{-2} mm^{-1}$		$q_p = 414/\left(A^{0.225} * (L*L_c/\sqrt{S_h})^{0.16} \right)$	–	107.98
Q_p	$m^3 s^{-1} mm^{-1}$	Peak discharge	$Q_p = A * q_p/1000$	–	1.20
V_b	m^3	Unit volume	$V_b = A * h_a * 1000$	–	11,080
T_b	hr	Base time	$T_b = (3.65 * V_b/Q_b)/3600$	–	9.39
T_p	hr	Time to peak discharge	$T_p = T_b/5$	–	1.88

Source: Ozdemir (1978).

ground control points (GCPs), acquisition of aerial images, and image processing.

3.2.1 | GCP establishments

Image orientation based on only geotags from navigation-grade global positioning system (GPS) receivers of UAVs may cause 10–20 m global shift of coordinates due to atmospheric conditions. This inaccuracy in GPS positioning cannot be reduced or detected by averaging geotagged images in image processing stage (Pix4D support site, 2018). The use of GCPs in image georeferencing is advised to reduce shifts due to GPS geotags from meters to centimetres (Kung et al., 2011; Mendes, Henriques, Catalao, Redweik, & Vieira, 2015). Hence, prior to UAV flights, the locations of 33 GCPs are designated as evenly as possible throughout the targeted mapping area. The latitude, longitude, and elevation of each point are measured with a Leica Viva GS15 GNSS receiver using the network of continuously operating reference stations, Turkey (CORS-TR), and they are marked temporarily with spray paint to be identified clearly in aerial

images. The geographic positions received by this GNSS device under the WGS84/UTM zone 36N coordinate system of 30 GCPs are utilised for refining the geolocation of the acquired aerial images, and three of them are used as check points in evaluating the absolute accuracy of the model to be generated.

3.2.2 | Aerial imagery acquisitions

A DJI Matrice 600 UAV-drone with a Zenmuse X5 camera mounted on a gimbal and equipped with a 15 mm DJI lens is utilised to conduct flight operations. This rotary-wing UAV has the advantages of vertical take-off and landing in confined spaces, hovering capability, and capturing vertical and tilted images by changing its orientation against fixed-wing-type UAVs (Suh & Choi, 2017). A notable deficiency of rotary-wing UAVs is their short flight duration because of their continuous battery consumption for revolving rotor blades continuously during flight operation (Siebert & Teizer, 2014). This limitation is overcome by using three sets of battery packs, each of which offers about 20–25 min of
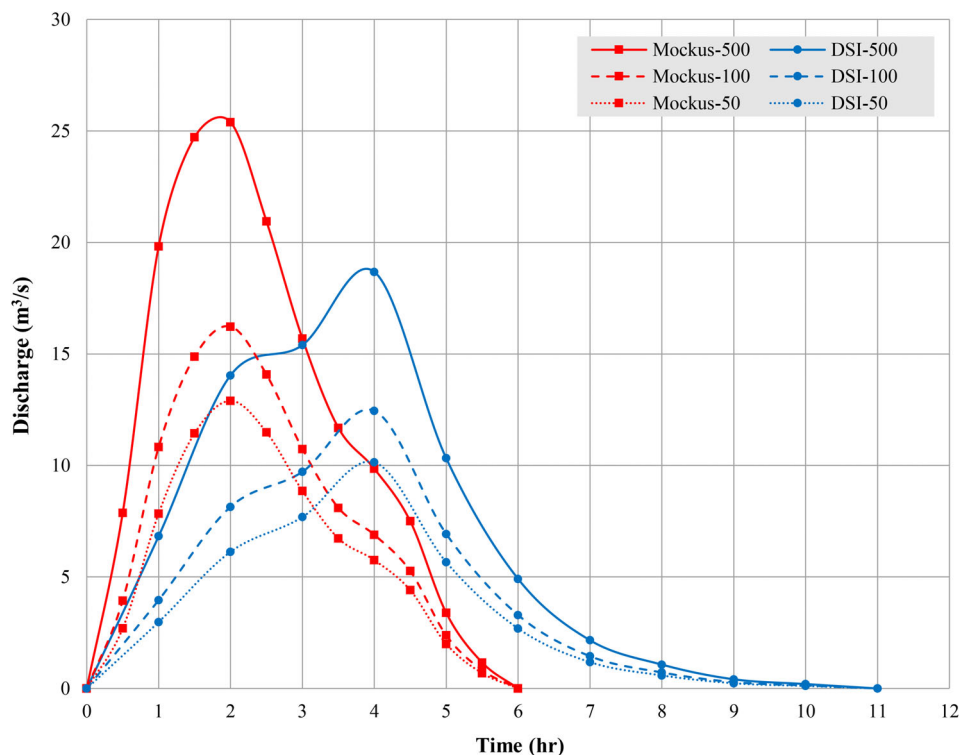
FIGURE 2 The 50-, 100- and 500-year flood hydrographs

flight time, to complete image acquisition process rapidly before the GCP markings are lost from view.

A flight plan for autonomous UAV navigation and image capture is formed using UgCS software (SPH Engineering, Riga, Latvia) prior to flight operations according to the remote-control range of the device and the designated six take-off locations in the mapping area. Auto-flight characteristics like image overlap percentages, flight altitude, cruise speed, and target ground sampling distance are added to the flight plan. Autonomous flights are conducted on 25 predefined flight paths at an altitude of 120 m above ground level with a speed of 5 m/s using a remote control connected to a smartphone running UgCS mobile application via wireless connection. Resultantly, 2,216 geotagged images with 60% forward overlap and 40% side overlap are obtained covering the whole target surface.

3.2.3 | Data processing

A combined photogrammetric processing of the acquired images is performed using Pix4DMapper Pro software (Pix4D S.A., Lausanne, Switzerland) with the inputted data on image properties, output coordinate system and desired model template for generating a DSM and an orthophoto. An initial processing is applied firstly to automatically extract scale-invariant key points on the images and then connect these points to each other over the overlapping parts of the images. After uploading the measured position data of all GCPs, the exact locations of 30 GCPs and three check points are assigned on multiple images in the *rayCloud* editor of the software by virtue of the spray paint markings on

the ground, and the process is reoptimized in terms of camera parameters to generate an accurately georeferenced sparse point cloud. Then, point cloud densification and mesh generation processes are applied to obtain a 3D point cloud consisting of approximately 600 million of points and a 3D textured mesh created by triangulation of these points in the densified point cloud. Finally, the DSM and orthophoto of the mapping region are generated using the DSM processing tool of the software, as presented in Figure 3a,b, respectively. The ground sampling distance of the produced DSM is 4.32 cm/pixel. When the differences between the location data of the pre-installed check points and their positions on the produced DSM are evaluated, the absolute accuracy of the model in root mean square error (RMSE) is calculated as 5.1 and 12.7 cm for the horizontal and vertical planes, respectively. The details of the applied image processing procedure in terms of system information, configuration options, and processing times are listed in Table 2.

Before using the generated DSM in 2D hydrodynamic model analyses, the terrain is modified for the existing flow obstructing structures, as the Hastane overpass on the D260 road, six road culverts on Kilicozu Creek, one pedestrian overpass on the D260 road, and five wooden bridges on Kilicozu Creek, shown in Figure 3b. In the remote-sensed topographical data of the UAV imagery, these structures appear as barriers through which water cannot pass. To ensure water flow through these hydraulically significant elements in flood simulations, they are removed initially from the base surface layer using HEC-RAS 5.0 software. After determining the dimensional and locational data of the
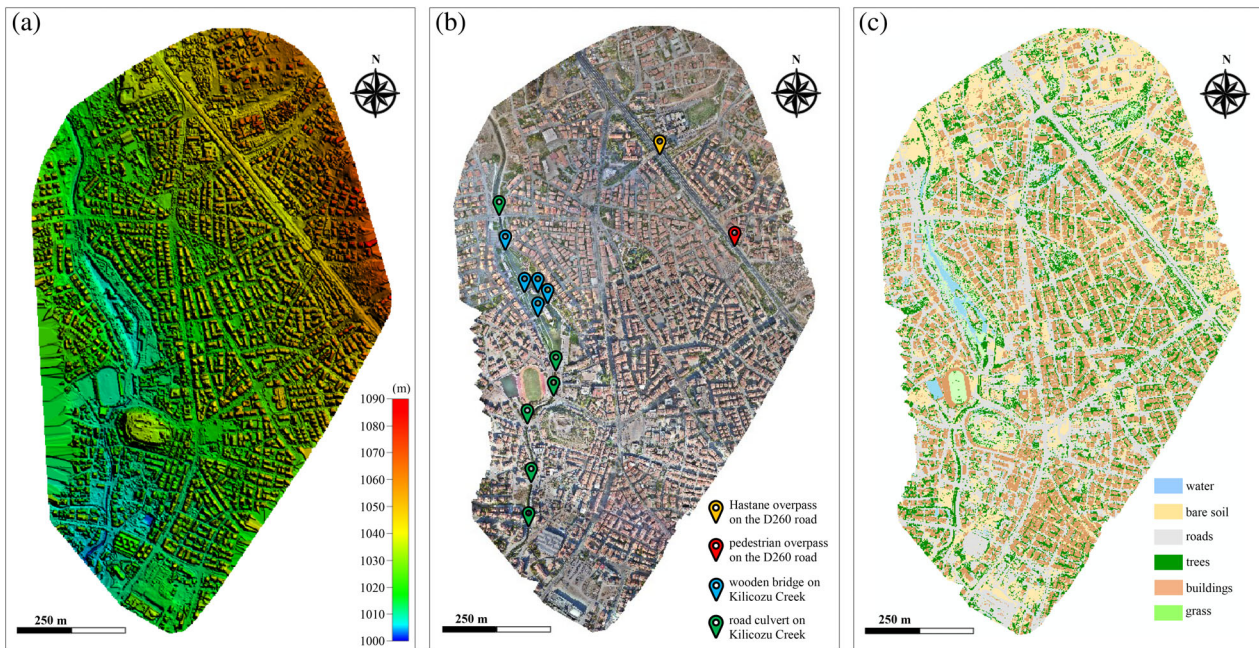
FIGURE 3   Results of UAV data processing (a) unmodified DSM; (b) orthophoto with the locations of the flow obstructing structures; (c) land cover map

subject structures determined by terrestrial measurements, a new terrain layer is created from the inputted cross-sections of the bare ground at each of the structure locations, and these two terrain layers are combined in the *RAS Mapper* interface of the software. Then, by applying the same procedure, these structures are remodelled excluding their decks on the combined terrain layer. The decks of these flow obstructing structures are not included in the remodelling process because openings between deck and bare ground cannot be introduced in the 2D modelling software to be utilised. The resultant DSM has the same raster cell size of the base surface model. Figure 4 shows an example of this modification for the Hastane overpass on the D260 road.

Land cover classification is performed on the orthophoto of the flood risk zone using the maximum likelihood classification tool of ArcGIS software (Environmental Systems Research Institute (ESRI), Redlands, California). A spatially varied land cover dataset is produced to differentiate six land features as water, bare soil, roads, trees, buildings, and grass, as shown in Figure 3c. The output raster cell size is selected as 0.1 m to increase the spatial accuracy in land classification and, hence, in Manning's roughness values to be assigned for the classified land features. This cell size can be changed while uploading the resultant land cover map into the hydrodynamic model interface according to computational cell size being used in the model development. Besides, after importing the resultant land cover map into the hydrodynamic model, misclassified regions can be overridden manually in the hydrodynamic model by defining new Manning's roughness polygons on the uploaded raster layer (Brunner and CEIWR-HEC, 2016).

3.3 | 2D hydrodynamic modelling through HEC-RAS 5.0

The inundation simulations for the 50-, 100-, and 500-year recurrence-interval floods are conducted through a 2D hydrodynamic model developed in HEC-RAS 5.0 software by using the produced DSM, orthophoto, and land cover map of the Kirsehir city center. In the modelling process, the modified terrain raster and orthophoto of the region are first uploaded into the *RAS Mapper* interface of the software, and a 2D flow area polygon representing the boundary of the flood risk zone is drawn on this terrain model in the *Geometric Data* editor of the software. In this drawing, the areas with low image overlaps at the boundaries of the terrain model are not included into the polygon. Then, a 2D computational mesh is automatically generated according to the entered 5 m × 5 m computational point spacing. The resultant mesh configuration consists of 107,139 grid cells having an average size of 25.08 m^2. This size is adequate to capture rapid changes in geometry and, therefore, in flow dynamics through such an urbanised region.

After the mesh generation, the upstream and downstream boundary condition lines are drawn along the outer boundary of the 2D flow area. The locations of boundary conditions are established at the mouth of the Hastane basin and at the far end of Kilicozu Creek for the upstream and downstream ends of flooding, respectively. The boundary condition types and related data are entered within the *Unsteady Flow Data* editor of the software. For the upstream boundary condition line, the flow hydrograph type boundary condition is utilised to bring flow into the simulation domain. The recurrence flood hydrograph produced with the 0.5-hr Mockus unit hydrograph is entered in 0.5-hr time intervals to simulate each flood scenario. Besides the flood hydrograph, it is

TABLE 2 System information and processing options in Pix4DMapper Pro software

Item	Description
System information	
Hardware	CPU: Intel Core i7-6700 processor operating at 3.40 GHz RAM: 32 GB GPU: NVIDIA GeForce GTX 1070
Operating system	Windows 10 Pro, 64-bit
Initial processing details	
Output coordinate system	WGS84/UTM zone 36N
Keypoints image scale	Full, image scale:1
Matching image pairs	Aerial grid or corridor
Matching strategy	Use geometrically verified matching: No
Keypoint extraction	Targeted number of keypoints: Automatic
Calibration	Calibration method: Standard Internal parameters optimization: All External parameters optimization: All Rematch: Automatic
Time for initial processing	02 h:52 m:54 s
Point cloud densification details	
Image scale	Multiscale, 1
Point density	Optimal
Minimum number of matches	3
3D textured mesh settings	Resolution: Medium Colour balancing: No Sample density divider: 1
Point cloud filters	Processing area, annotations
Time for point cloud densification	18 h:13 m:52 s
Time for 3D textured mesh generation	01 h:18 m:45 s
DSM and orthophoto generation details	
DSM and orthophoto resolution	Automatic: 1 × GSD
DSM filters	Noise filtering, surface smoothing (sharp)
Raster DSM	Method: Inverse distance weighting Merge tiles: Yes
Orthophoto	Merge tiles: Yes
Time for DSM generation	06 h:27 m:05 s
Time for orthophoto generation	02 h:12 m:23 s

required to define an energy slope for computing normal depth along the boundary condition line for each computational time step (Brunner and CEIWR-HEC, 2016). The energy slope is determined as 0.030 m/m by assuming that it is equal to the bed slope near the upstream boundary condition line. The normal depth type boundary condition is used for the downstream boundary condition. The required friction slope value for this type boundary condition is determined as 0.010 m/m considering the land slope in the vicinity of the downstream boundary condition line.

The next step is the assignment of Manning's roughness values for each land use type in the 2D flow area. The produced land cover raster with 0.1 m cell size is uploaded into the *RAS mapper* interface by converting the cell size to 5 m

to be the same as the computational cell size. The roughness values are assigned as 0.050, 0.030, 0.020, 0.150, 10, and 0.035 for the pre-defined water, bare soil, roads, trees, buildings, and grass classes, respectively (Chow, 1959). To override the assigned roughness values of the misclassified regions on the land cover layer, 2D flow area Manning's roughness polygons are drawn manually on the orthophoto of the region in the *Geometric Data* editor of the software. Besides, the concrete-lined with sides of cement rubble masonry and glazed tile-lined sections of Kilicozu Creek are separated from the feature class defined as water for natural creek sections by assigning 0.025 and 0.015, respectively, as new roughness coefficients (Chow, 1959).

After defining all the terrain features of the 2D flow area visually as shown in Figure 5, the computational mesh is preprocessed to develop hydraulic property tables. When the 2D geometric preprocessor in the *RAS mapper* interface is run, elevation-volume relationship for each cell and elevation-hydraulic properties (area, wetted perimeter, and roughness) relations for each cell face are computed and inscribed into the hydraulic property tables. The movement of water into, through, and out of a cell is controlled by the data in these tables, and this control allows water to flow through only a portion of the cell without covering the entire cell surface. Although the usage of larger computational cells keeps all the topographical features of the terrain they covered, the assigned Manning's roughness value for each cell face is based on the roughness data at the cell face center, not at the other parts of the cell face or at any points in the cell area (Brunner and CEIWR-HEC, 2016). Thus, the use of a land cover layer having a smaller cell size than the computational cell size does not contribute to improve the model accuracy.

The last step of the model development is the determination of calculation options for unsteady flow simulations within the *Unsteady Flow Analysis* editor of the software. The software has the capability to perform 2D unsteady flood routing with either the full momentum (Saint Venant) equations or the diffusion wave equations. Although the full momentum equations need a smaller computation time interval and, therefore, a much higher computation time than the diffusion wave equations, the usage of the full momentum equation set is advised to obtain more accurate results (Brunner and CEIWR-HEC, 2016). In this assessment, the full momentum equations are utilised with 0.1-s computational time step considering the model stability according to the Courant–Friedrichs–Lewy condition (Brunner and CEIWR-HEC, 2016; Courant, Friedrichs, & Lewy, 1928). Besides, the initial conditions time option advised by Brunner and CEIWR-HEC (2016) for 2D flow areas having flow or stage hydrograph type external boundary conditions, is utilised for ramping the 2D boundary conditions up from zero to their initial values. The initial conditions time is set to be 3 hr by conducting trial simulations to determine an

FIGURE 4   An example for DSM modifications (a) Hastane overpass on the D260 road; (b) unmodified DSM section; (c) modified DSM section

approximate value for the travel time of the first flood wave from the upstream to downstream ends of flooding. The recurrence flood scenarios are simulated with a model output time interval of 1 min, and the model provides the extent of inundated area, inundation depths, flow velocities, and arrival times for each flood scenario in a spatially distributed way.

4 | RESULTS AND DISCUSSIONS

The developed model is run under the 2D hydrodynamic unsteady flow condition for each of the 50-, 100-, and 500-year recurrence-interval floods. The simulation duration is taken as 6 hr for all flood scenarios according to the base time of the recurrence flood hydrographs, and the other modelling parameters are considered as per the previous section. The model runs are performed on a Windows 10 (64 bit) notebook equipped with an Intel Core i7-6700HQ processor operating at 2.60 GHz, 16 GB memory, and a NVIDIA GeForce GTX 960 M graphics card. The time spent for unsteady flow computations in 0.1-s time

intervals during the 6-hr simulation period are 482, 498, and 569 min for the 50-, 100-, and 500-year recurrence-interval flood scenarios, respectively.

Figures 6–8 demonstrate the simulation outputs taken at every 1-min interval for the 50-, 100-, and 500-year floods, respectively. The result shows that the risky zone assumption is consistent with the spatial distribution of the flooded areas. The canal capacity of Kilicozu Creek seems to be adequate to discharge flood waters in all flood scenarios, and the decrease in the probability of flooding does not considerably change the extent of inundation area in the city center (Figures 6a, 7a, 8a). On the other hand, it is observed that the other simulation outputs, namely, inundation depths, flow velocities, and arrival times, vary considerably with respect to the inputted flow hydrographs, unlike the flooding extents.

In the 50-year flood scenario, the obtained inundation depths at some critical locations in the city centre such as the D260 road, the Ankara street, the Kentpark recreation area, the Boztepe playground, the Masal playground, and the Ahi Evran mosque are 0.2, 0.3, 0.3, 1.0, 0.5, and 0.4 m, respectively. However, these depths reach 0.3, 0.6, 0.4, 1.4, 0.6,

FIGURE 5 Geometric data representation in HEC-RAS 5.0 software

and 0.6 m at the same locations in the 500-year scenario. Besides, while the obtained water depth in the glazed tile-lined sections of the Kilicozu Creek inside the Kentpark recreation area is around 1.6 m in the 50-year flood scenario, this depth rises to 3.0 m in the 500-year flood scenario, resulting in the inundation of the surrounding areas inside the Kentpark region (Figures 6b, 7b, 8b).

Actually, the major factors that would affect the severity of damage in terms of human life for this risk zone are the velocity and arrival time of flood waters. According to the simulation outputs for the 500-year flood hydrograph, the flow velocities at the D260 road, the Ankara street, the Kentpark recreation area, the Boztepe playground, the Masal playground, and the Ahi Evran mosque can rise to 2.0, 1.1, 0.6, 1.4, 1.1, and 1.2 m/s, respectively. There are some other high-risk regions with intense pedestrian and vehicle traffic where the flow velocities can reach 3.1 m/s (Figures 6c, 7c, 8c). Besides, the surface runoff seems to occur only 12 and 48 min later than the start of a 4-hr rainfall event resulting in a 50-year flooding at the Boztepe playground and the D260 road, respectively. This time is less than 2 hr for the other locations in the extent of flooding. As the probability of

flood occurrence decreases, the arrival times of flooding become much shorter (Figures 6d, 7d, 8d).

Although many studies in the literature have highlighted that higher resolution DSMs produce more accurate flood maps when compared to coarser resolution DSMs which overpredict the flood inundation extents, the use of a high-resolution DSM with centimetre-scale localization accuracy in the model development is not enough alone to indicate that the model outputs are reliable (Cook & Merwade, 2009; Marks & Bates, 2000; Omer, Nelson, & Zundel, 2003; Saksena & Merwade, 2015). It is unknown how the uncertainties associated with precipitation, flood hydrographs, modelling parameters and techniques, and geospatial operations affect the overall accuracy of generated flood hazard maps (Merwade, Olivera, Arabi, & Edleman, 2008). Thus, there is no possibility of verifying the obtained simulation results due to the lack of records of past flood events. The hydraulics of monitored floods is indispensable for the calibration process of the generated 2D hydrodynamic model. Inundation data of at least two past flood events, including inundation depths, flow velocities, and arrival times measured at several locations, extent of inundation, time of occurrence, flood duration, and stage hydrograph of Kilicozu Creek, are required to perform first a model calibration with the records of a flood event in terms of the assigned roughness values to the land cover classes and then a validation process for the calibrated model with the data of another flood event.

Although the model outputs cannot be relied upon alone without calibrating the generated model with observed flooding data, these results are useful for such a preliminary assessment that reveals the flash flood risk in the Kirsehir city center from the mountainous region in the north of the city. There is no doubt that some number is better than no number to raise awareness against the unexpected effects of possible flood events that an intermittent stream can cause. Even if the 2D hydrodynamic model is not calibrated, the use of a high-resolution DSM in the model generation provides the opportunity to obtain cautionary outcomes on the movement of flood water for taking appropriate flood risk mitigation measures. For instance, when the movements of water obtained for the simulated flooding scenarios are analysed from the Hastane basin outlet through the urbanised area into Kilicozu Creek, the Boztepe playground area can be identified as the most risky part of the whole floodplain. This pit area acts as a retarding reservoir. After the flood waters fill this area, they pass across the D260 road and begin to inundate the city center. Hence, the first measure to be taken against the risk of flooding should be the removal of this playground. Besides, one or more retarding reservoirs should be constructed in the Hastane catchment for the temporary storage of flood waters which are subsequently released as
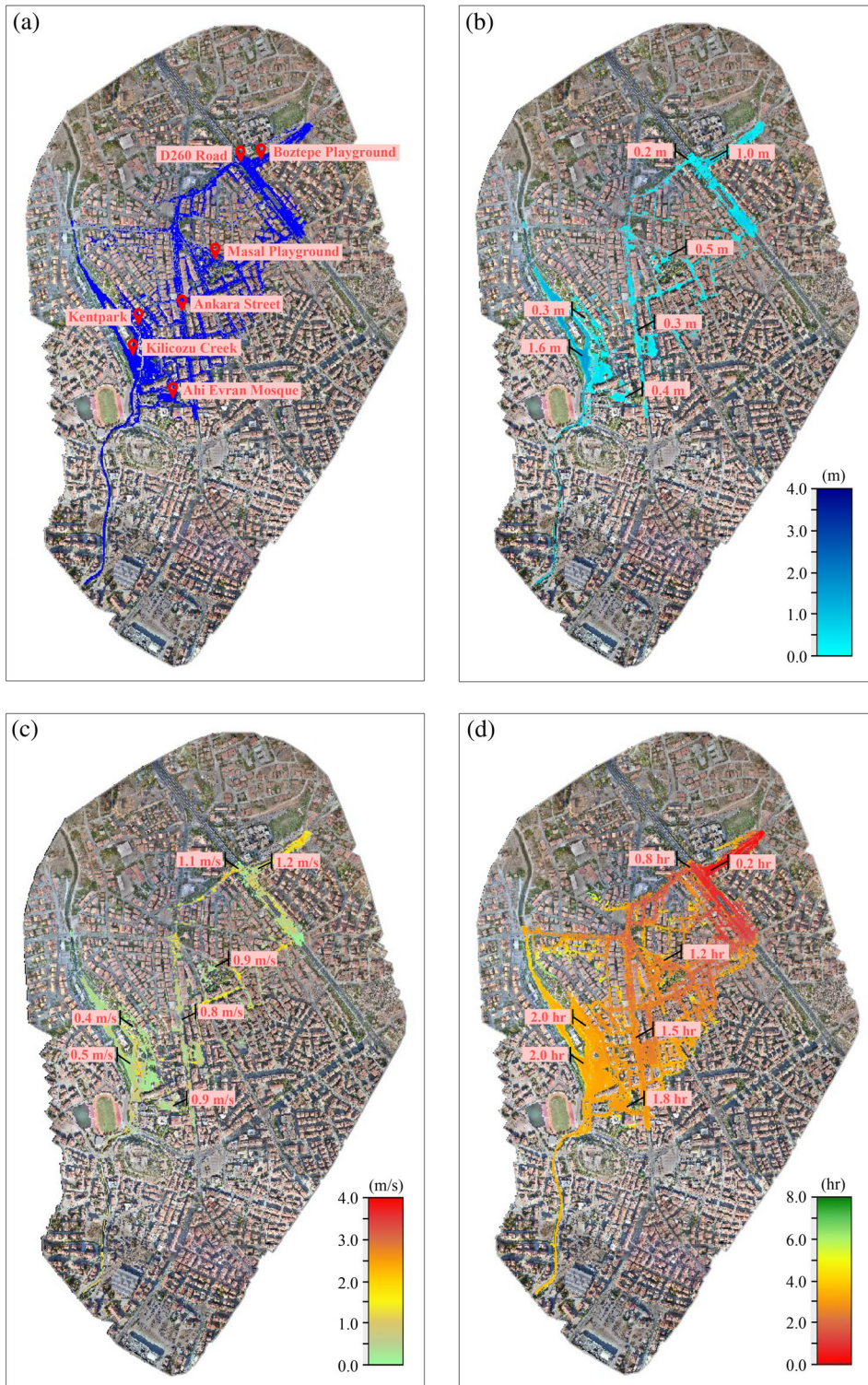
FIGURE 6 The 50-year recurrence flood scenario (a) flood extent; (b) inundation depths; (c) flow velocities; (d) arrival times

rapidly as inundation conditions in the city center would permit.

5 | CONCLUSIONS

This study presents the steps carried out to generate flood inundation maps for the case of the Kirsehir city center using 2D hydrodynamic modelling under data scarcity. In the absence of measured flow data, the produced flood scenarios are only based on the annual maximum 24-hr precipitation records, and the recurrence flood hydrographs are estimated with the synthetic unit hydrograph methods considering the empirical relationships of the physical catchment characteristics. The absence of flood records even about water levels and inundation extents that can be
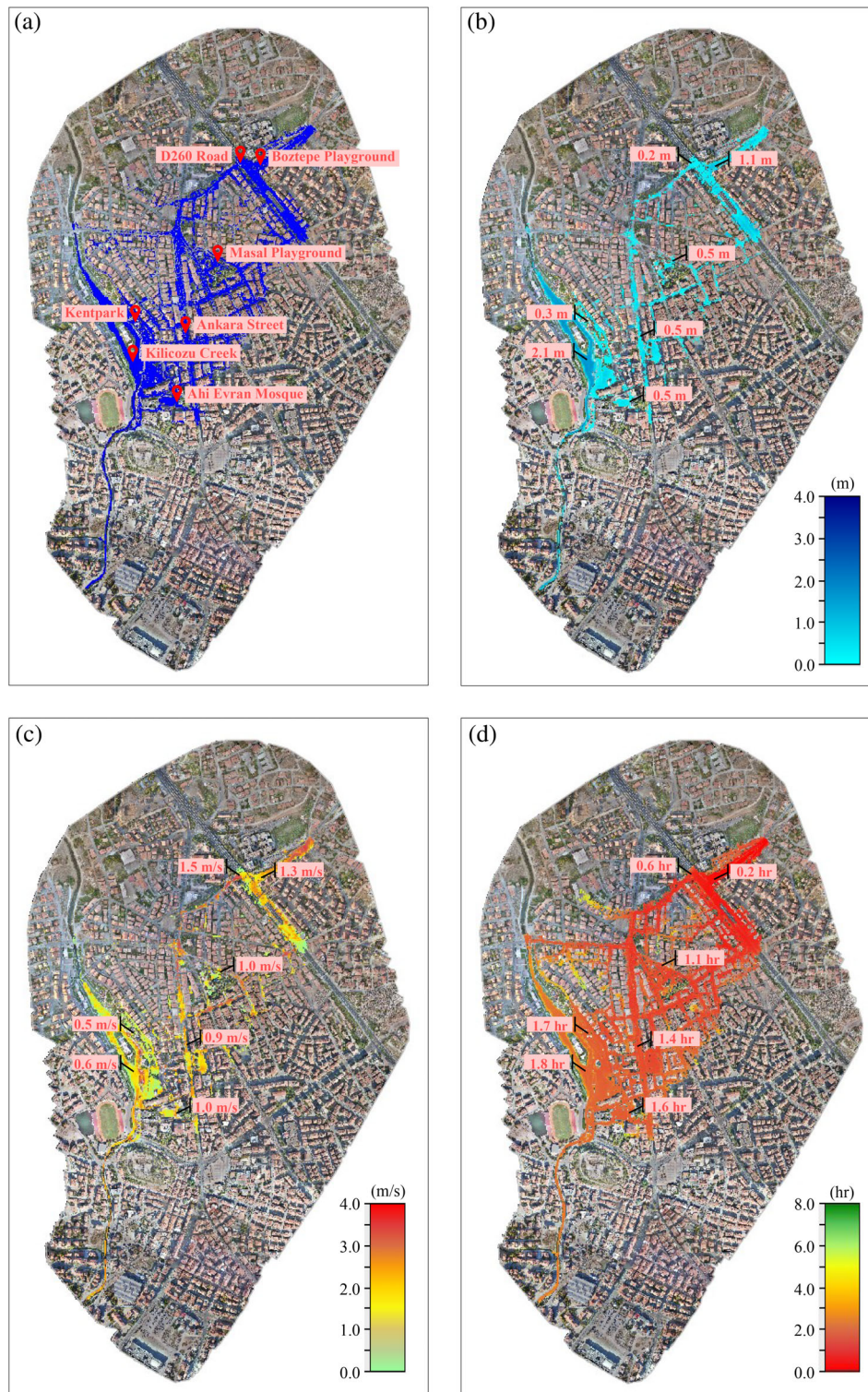
FIGURE 7   The 100-year recurrence flood scenario (a) flood extent; (b) inundation depths; (c) flow velocities; (d) arrival times

used in model calibration and verification makes it necessary to utilise high-quality data as much as possible in model development. Hence, at least to simulate flow movement more accurately through a model that cannot be calibrated due to lack of data, a high-resolution DSM produced with a high order of spatial accuracy by processing the aerial images acquired by the UAV flights over the flood risk zone is utilised in model development. Besides,

the orthophoto of the mapping area generated by integrating the aerial images is classified to produce a spatially varied land cover dataset to be used in assigning roughness coefficients to the flow area.

The conducted 2D hydrodynamic model simulations demonstrate how urbanisation and settlement in flood prone areas can turn a "natural" flood event into a disaster. Although the semi-arid climate and long series of floodless
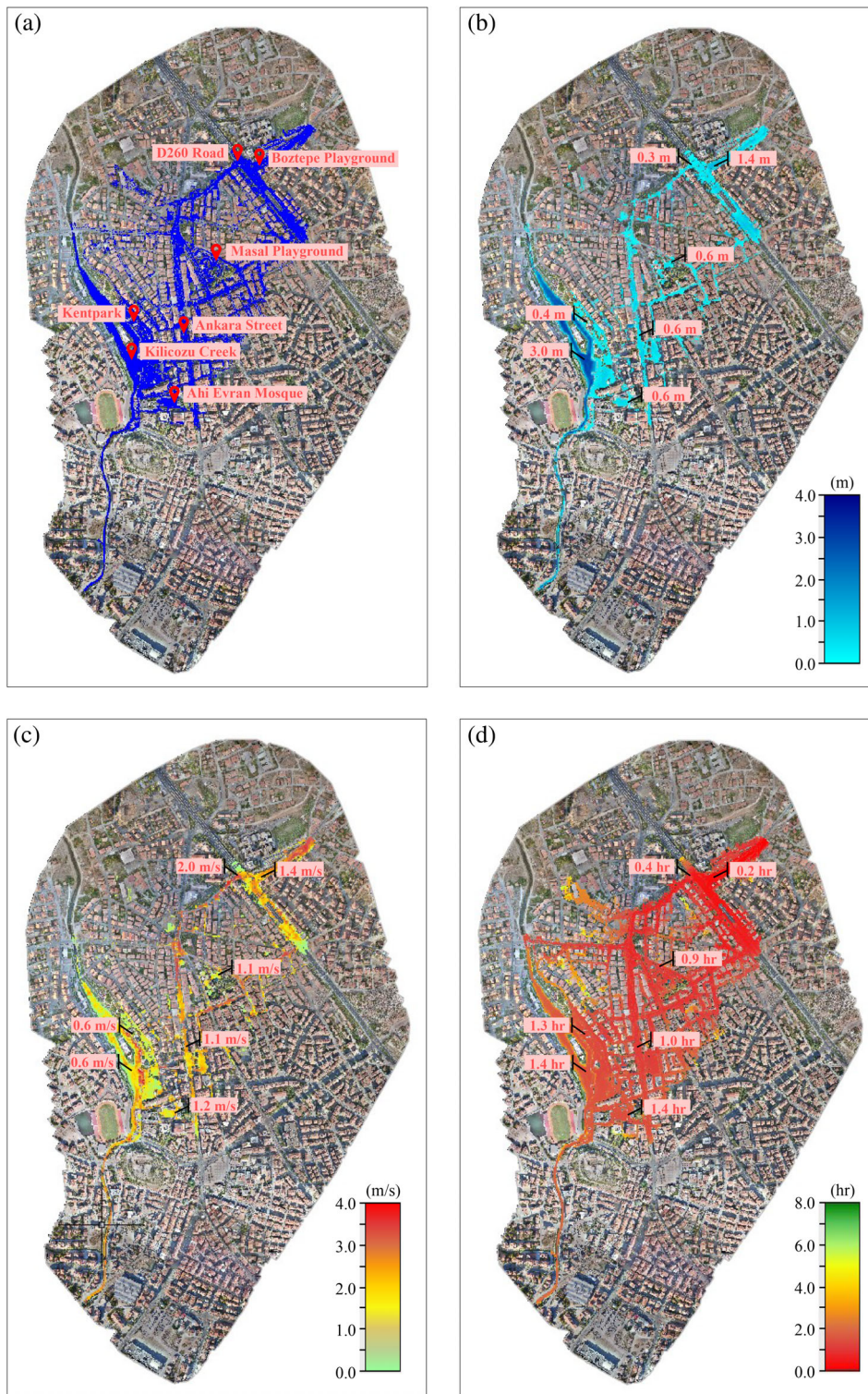
FIGURE 8 The 500-year recurrence flood scenario (a) flood extent; (b) inundation depths; (c) flow velocities; (d) arrival times

years has encouraged the provincial authorities and local settlers to downplay the flood risk from such an intermittent stream draining a relatively small mountainous watershed, the risk appears to be higher than in the past due to the impacts of climate change on rainfall regimes. The resultant flood hazard maps provide the ability to accurately predict areas exposed to flash flooding that would guide in planning structural and non-structural measures to protect these areas

from future damage and guide in planning the growth of the city center. It is hoped that this study will raise awareness on flash flood risk and its management.

ORCID

Emrah Yalcin https://orcid.org/0000-0002-3742-8866

REFERENCES

Anees, M. T., Abdullah, K., Nawawi, M. N. M., Rahman, N. N. N. A., Piah, A. R. M., Zakaria, N. A., … Omar, A. K. M. (2016). Numerical modeling techniques for flood analysis. *Journal of African Earth Sciences*, *124*, 478–486.

Brunner, G. W., & CEIWR-HEC. (2016). *HEC-RAS river analysis system, 2D modeling user's manual*. Davis, CA: US Army Corps of Engineers Institute for Water Resources Hydraulic Engineering Center.

Casas, A., Benito, G., Thorndycraft, V. R., & Rico, M. (2006). The topographic data source of digital terrain models as a key element in the accuracy of hydraulic flood modelling. *Earth Surface Processes and Landforms*, *31*(4), 444–456.

Chow, V. T. (1959). *Open channel hydraulics*. New York, NY: McGraw-Hill.

Colomina, I., & Molina, P. (2014). Unmanned aerial systems for photogrammetry and remote sensing: A review. *ISPRS Journal of Photogrammetry and Remote Sensing*, *92*, 79–97.

Cook, A., & Merwade, V. (2009). Effect of topographic data, geometric configuration and modeling approach on flood inundation mapping. *Journal of Hydrology*, *377*(1–2), 131–142.

Courant, R., Friedrichs, K., & Lewy, H. (1928). Uber die partiellen differenzengleichungen der mathematischen physik. *Mathematische annalen*, *100*, 32–74 (in German).

Dankers, R., & Feyen, L. (2009). Flood hazard in Europe in an ensemble of regional climate scenarios. *Journal of Geophysical Research*, *114*(D16108), 1–16.

Dein, M. A. (1985). *Estimation of floods and recharge volumes in wadis Fatimah, Na'man and Turabah.* (Unpublished M.Sc. thesis). King Abdulaziz University, Jeddah, Saudi Arabia.

DSI. (1989). *Preliminary investigation report on the flood protection strategy of the Kirsehir city center*. Kayseri: XIIth Regional Directorate of State Hydraulic Works (in Turkish).

Els, Z., & Van Niekerk, A. (2013). Data availability and requirements for flood hazard mapping. *PositionIT*, *44*, 1–8.

Eren, M. E. (2011). *Investigations on the flood risk of the Bogluca (Kayali) stream.* (M.Sc. thesis). Yildiz Technical University, Istanbul, Turkey. (in Turkish).

Feng, Q., Liu, J., & Gong, J. (2015). Urban flood mapping based on unmanned aerial vehicle remote sensing and random forest classifier – A case of Yuyao, China. *Water*, *7*(4), 1437–1455.

Ghoneim, E., & Foody, G. M. (2013). Assessing flash flood hazard in an arid mountainous region. *Arabian Journal of Geosciences*, *6*(4), 1191–1202.

Kung, O., Strecha, C., Beyeler, A., Zufferey, J.-C., Floreano, D., Fua, P., & Gervaix, F. (2011). The accuracy of automatic photogrammetric techniques on ultra-light UAV imagery. *The International Archives of the Photogrammetry, Remote Sensing and Spatial Information Sciences*, *38*(1 C22), 125–130.

Langhammer, J., Bernsteinova, J., & Mirijovsky, J. (2017). Building a high-precision 2D hydrodynamic flood model using UAV photogrammetry and sensor network monitoring. *Water*, *9*(11), 861.

Liu, Q., Qin, Y., Zhang, Y., & Li, Z. (2015). A coupled 1D–2D hydrodynamic model for flood simulation in flood detention basin. *Natural Hazards*, *75*(2), 1303–1325.

Marks, K., & Bates, P. (2000). Integration of high-resolution topographic data with floodplain flow models. *Hydrological Processes*, *14*(11–12), 2109–2122.

Mendes, T., Henriques, S., Catalao, J., Redweik, P., & Vieira, G. (2015). Photogrammetry with UAV's: Quality assessment of open-source software for generation of orthophotos and digital surface models. In *Proceedings of VIII Conferencia Nacional De Cartografia e Geodesia*. Lisbon, Portugal: Ordem dos Engenheiros.

Merwade, V., Olivera, F., Arabi, M., & Edleman, S. (2008). Uncertainty in flood inundation mapping: Current issues and future directions. *Journal of Hydrologic Engineering*, *13*(7), 608–620.

MGM. (2017a). *Annual maximum precipitation records in standard times for the Kirsehir Station*. Ankara, Turkey: Turkish State Meteorological Service.

MGM. (2017b). *Lon-term all parameters bulletin for the Kirsehir Station*. Ankara, Turkey: Turkish State Meteorological Service.

Omer, C. R., Nelson, E. J., & Zundel, A. K. (2003). Impact of varied data resolution on hydraulic modeling and floodplain delineation. *Journal of the American Water Resources Association*, *39*(2), 467–475.

Ozdemir, H. (1978). *Applied flood hydrology*. Ankara, Turkey: General Directorate of State Hydraulic Works (in Turkish).

Papaioannou, G., Loukas, A., Vasiliades, L., & Aronica, G. T. (2016). Flood inundation mapping sensitivity to riverine spatial resolution and modelling approach. *Natural Hazards*, *83*(1), 117–132.

Pix4D support site. (2018). *How the onboard GPS affects the accuracy of a project?* Retrieved from https://support.pix4d.com/hc/en-us/articles/202558909#gsc.tab=0.

Quiroga, V. M., Kure, S., Udo, K., & Mano, A. (2016). Application of 2D numerical simulation for the analysis of the February 2014 Bolivian Amazonia flood: Application of the new HEC-RAS version 5. *RIBAGUA*, *3*(1), 25–33.

Saksena, S., & Merwade, V. (2015). Incorporating the effect of DEM resolution and accuracy for improved flood inundation mapping. *Journal of Hydrology*, *530*, 180–194.

Sanders, B. F. (2007). Evaluation of on-line DEMs for flood inundation modeling. *Advances in Water Resources*, *30*(8), 1831–1843.

Schumann, G., Matgen, P., Cutler, M. E. J., Black, A., Hoffmann, L., & Pfister, L. (2008). Comparison of remotely sensed water stages from LiDAR, topographic contours and SRTM. *ISPRS Journal of Photogrammetry and Remote Sensing*, *63*(3), 283–296.

Sen, Z. (2018). *Flood modeling, prediction and mitigation*. Cham, Switzerland: Springer.

Serban, G., Rus, I., Vele, D., Bretcan, P., Alexe, M., & Petrea, D. (2016). Flood-prone area delimitation using UAV technology, in the areas hard-to-reach for classic aircrafts: Case study in the north-east of Apuseni Mountains, Transylvania. *Natural Hazards*, *82*(3), 1817–1832.

Siebert, S., & Teizer, J. (2014). Mobile 3D mapping for surveying earthwork projects using an unmanned aerial vehicle (UAV) system. *Automation in Construction*, *41*, 1–14.

Smith, M. J., Edwards, E. P., Priestnall, G., & Bates, P. (2006). *Exploitation of new data types to create digital surface models for flood inundation modeling*. Manchester, England: Flood Risk Management Research Consortium.

Suh, J., & Choi, Y. (2017). Mapping hazardous mining-induced sinkhole subsidence using unmanned aerial vehicle (drone) photogrammetry. *Environmental Earth Sciences*, *76*(4), 144.

Teng, J., Jakeman, A. J., Vaze, J., Croke, B. F. W., Dutta, D., & Kim, S. (2017). Flood inundation modelling: A review of methods, recent advances and uncertainty analysis. *Environmental Modelling & Software*, *90*, 201–216.

Tsubaki, R., & Fujita, I. (2010). Unstructured grid generation using LiDAR data for urban flood inundation modelling. *Hydrological Processes*, *24*(11), 1404–1420.

Usul, N. (2009). *Engineering hydrology*. Ankara, Turkey: METU Press.

Zevenbergen, C., Cashman, A., Evelpidou, N., Pasche, E., Garvin, S., & Ashley, R. (2010). *Urban flood management*. Boca Raton, FL: CRC Press.